




Upscaling of transport through discrete fracture networks via random walk: A comparison of models

Nicole L. Sund * and Rishi Parashar *Division of Hydrologic Sciences, Desert Research Institute, Reno, Nevada 89512, USA*

Hai V. Pham

Division of Hydrologic Sciences, Desert Research Institute, Las Vegas, Nevada 89119, USA (Received 12 September 2019; revised 14 January 2021; accepted 7 May 2021; published 14 June 2021)

Many models have been created for upscaled transport modeling in discrete fracture networks (DFNs). Random walk examples of these are the Markov directed random walk (MDRW), Monte Carlo solution of the Boltzmann transport equation (BTE), and the spatial Markov model (SMM). Each model handles the correlation between the random walk steps using different techniques and has successfully reproduced the results of full-resolution transport simulations in DFNs. However, their predictive capabilities under different modeling scenarios have not been compared. We construct a set of random 2D DFNs for three different fracture transmissivity distributions to comparatively evaluate model performance. We focus specifically on random walk models to determine what aspects of the space and time step distributions (e.g., correlation and coupling) must be accounted for to get the most accurate predictions. For DFNs with low heterogeneity in fracture transmissivity, accounting for correlation generally leads to less accurate predictions of transport behavior, but as the fracture transmissivity distribution widens, preferential pathways form and correlation between modeling steps becomes important, particularly for early breakthrough predictions.

DOI: [10.1103/PhysRevE.103.062116](https://doi.org/10.1103/PhysRevE.103.062116)

I. INTRODUCTION

Flow and transport in fractured rock are often characterized by a wide range of velocities. The velocity of solute within the fracture network can be several orders of magnitude higher than the velocity of solute within the surrounding rock matrix [1,2]. This makes numerical solution of the transport behavior computationally intensive because high gradients require fine grids.

To model flow and transport in fractured rock, it is often desirable to upscale via some type of averaging procedure so that the fine details of the flow are accounted for in an effective way rather than explicitly resolved. For flow, this can be done by establishing effective hydraulic conductivity tensors that account for interconnected sets of fractures [3–6] or the coupled influences of both the fractures and the matrix [7,8].

For transport, however, this type of approach is insufficient. The use of effective hydraulic conductivity in transport models leads to the use of an advection dispersion equation, which assumes that transport is Fickian. Variations in small-scale velocity lead to enhanced spreading of the solute (as defined by the change in the variance of the solute plume), which scales faster than linear in time until it asymptotes to linear spreading. If the area of the domain over which the effective hydraulic conductivity is defined is large enough for this asymptotic behavior to occur, then this approach is valid

[3]. However, the higher the variation in velocity, the larger the region must be for the transport within it to become Fickian.

An alternative approach is to model transport only within the high-velocity regions of the flow. In fractured rock, this is done using discrete fracture network (DFN) models, which assume no flow within the rock matrix [9–11]. This approach gives a more accurate description of transport within the fractures, but is restricted to small-scale use because of computational expense. Therefore, there is a need for upscaling models that can accurately extrapolate the transport behavior from small-scale DFNs to larger scales.

Many models, both Lagrangian and Eulerian, have been created for and applied to upscaled transport modeling in DFNs. In this work, we focus specifically on Lagrangian random walk models, each of which uses particle trajectories from the DFN simulations to create empirical space and time step distributions that are sampled from for the random walk simulations. In a broad sense, these models can all be categorized as continuous time random walk (CTRW) models [12–14], but the models have different definitions of what constitutes a “step” and have different ways of modeling the correlation between steps. The three models we focus on are the Markov directed random walk (MDRW) [10], the Monte Carlo solution of the Boltzmann transport equation (BTE) [16], and the spatial Markov model (SMM) [15]. Each model has had success in reproducing the results of full resolution transport simulations in DFNs [10,16,17], but this is the first side-by-side comparison of the predictive capability of these models in both correlated and uncorrelated forms. All models account for the correlation between steps using a Markov

*nsund@dri.edu

chain; the correlated forms of the models use multistate Markov chains with state-dependent probabilities (Markov-1), whereas the uncorrelated forms use trivial Markov chains with either a single-state probability or the same probability distribution for each state (Markov-0). The hypothetical case study used to compare these models is a set of realizations of random 2D DFNs for three different fracture transmissivity distributions. As the variance of the transmissivity distribution increases, the range of velocities within the DFN widens while the number of high flux fractures decreases [11,18]. This can have a profound effect on the predictive capability of the upscaled models, particularly with regard to comparisons between correlated and uncorrelated models. The goal of this study is to investigate the predictive capability of these three random walk models to determine what aspects of the space and time step distributions (e.g., correlation and coupling) must be accounted for to inform model choice for fractured systems. To keep the analysis simple, we do not perturb the injection modes or change the initial velocity distribution at the inlet, which are factors shown to have a strong impact on transport in DFNs and performance of upscaling methods [19–21]. The potential effect of the velocity distribution at the inlet is minimized in our study by restricting the injection region to a small source area rather than an entire inlet plane.

The capability of the upscaled models to predict transport in real fractured rock depends on both the accuracy of the DFN simulations and on how well the upscaled models match the DFN simulations. The scope of this work is limited to the latter. For our purposes, we assume the transport results of the DFN simulations are accurate and try to match upscaled models to these simulations. The upscaled models are analyzed based on how well they match DFN simulations. This approach can be used to assess the predictive capabilities of the models, assuming the DFN simulations are accurate. Upscaled modeling allows for transport behavior of smaller scale DFNs to be extrapolated to larger scale DFNs (which are very computationally expensive). For the interested reader, the development of a 2D DFN flow and transport simulation is provided in Ref. [11].

The use of 2D DFN models in this study is intended to serve as the foundation for developing and evaluating transport upscaling methods in 3D DFNs. Three-dimensional flow and transport simulations differ from their 2D counterparts in many ways, but for the upscaled models to be considered robust, they should be capable of predicting transport in both situations. Some recent work on transport upscaling for 3D DFNs shows the promise of a Bernoulli CTRW [19,22], but also highlights the limitations (underestimation of early solute arrival time and overestimation of late-time arrival) for networks with high aperture variation and different correlation lengths [21]. Bernoulli model predictions improve when local network topological features (tortuosity distribution) are included in the upscaling framework [22]. Use of an average advective tortuosity, a parameter which is sensitive to aperture heterogeneity and injection modes, leads to poor upscaled transport predictions [21]. Parametrization of local topological features is difficult, hence there is a need to evaluate applicability and performance of progressively sophisticated CTRW models in both uncorrelated and correlated modes for DFNs. With the increased computational expense of 3D flow

and transport simulations, we hope to establish a framework for evaluating model responses and eliminate some of the candidate models before extending the upscaling techniques to 3D in a future study.

The manuscript is organized into six sections as follows. First, we describe the DFN simulations in Sec. II, including the effect of widening the distribution of fracture transmissivity and the information we collect to parametrize the upscaled models. Next, we describe the upscaled modeling in Sec. III. Then, we discuss the modeling results for both correlated and uncorrelated versions of the models, with varying modeling scales, in Sec. IV. Finally, we discuss the relevance of the results with regard to future modeling efforts in Secs. V and VI.

II. DISCRETE FRACTURE NETWORK (DFN) SIMULATIONS

We run DFN simulations at both large and small scales to test and parametrize the set of upscaled transport models. Large-scale DFN simulations are used to create detailed transport behavior, which we hope to predict using the upscaled models. Another set of transport simulations is done on a smaller region of the DFN, in which information on the trajectory of particles is collected and analyzed to create empirical space and time step distributions that are used to develop upscaled predictions of the large-scale DFN transport using each upscaled random walk model. All fracture networks are generated and flow is solved using a numerical DFN generator, solver, and transport simulator [11].

A. DFN simulation setup

The first step is to create the large-scale fracture network itself. We assume that the matrix is of negligible permeability and flow only takes place in connected sets of fractures. Discrete fracture networks are stochastically generated through the incremental addition of fractures with statistically defined random location, length, and orientation until a specified density criterion is reached [11]. Fracture network density is defined as the total length of all fractures normalized by the domain area. Fractures may intersect boundaries or other fractures and we define a fracture segment as the portion of a fracture between two intersections [13,14]. The network is split into segments and isolated fractures and dead-end segments are identified and deleted because they are not hydraulically connected to the boundaries, and therefore cannot convey any flow. Several analyses of field data have determined that fracture trace length often follows a power law distribution [3,23–26]. The assumption that DFNs are scale free underlies the use of power law distributions for fracture trace length. Studies indicate that the values of the power law exponent, α , typically range between 1 and 3 for natural rock fracture networks [23,24,26]. Fracture angles are drawn from a Von Mises distribution, which is analogous to a normal distribution on a circle [27]. In this work, fracture density is $1/2 \text{ m/m}^2$ and domain size is fixed at $1000 \times 200 \text{ m}$. Table I shows the probability density function (PDF) of each fracture characteristic used in this work. Figure 1 shows a realization of the DFN, before removal of isolated segments.

TABLE I. Distribution of fracture characteristics.

Characteristic (X)	Distribution	PDF [$f_X(x)$]	Parameters
Length [m]	Pareto	$\frac{\alpha x_{\min}^\alpha}{x^{\alpha+1}}$ $x \geq x_{\min}$ 0 $x < x_{\min}$	$x_{\min} = 2$ m $\alpha = 1.5$
Angle [radians]	Von Mises	$\frac{\exp[\kappa \cos(x-\mu)]}{2\pi I_0(\kappa)}$	$\kappa = 20$ $\mu^b = \{0, \frac{\pi}{2}\}$
Transmissivity [$\frac{m^2}{s}$]	Log-normal	$\frac{1}{x\sigma\sqrt{2\pi}} \exp\left(-\frac{(\ln x - \mu)^2}{2\sigma^2}\right)$	$\mu = -10$ $\sigma^c = \{0, 0.5, 1\}$

^a $I_0(\kappa)$ is the zeroth-order modified Bessel function of the first kind.

^bTwo equiprobable sets of fractures are generated with $\mu_1 = 0$ and $\mu_2 = \frac{\pi}{2}$, respectively.

^c σ varies between sets of DFNs.

The only fracture characteristic parameter we vary between DFNs is the standard deviation, σ , of the transmissivity distribution. When $\sigma = 0$, the transmissivity of all fractures are the same, but as σ increases the range of fracture transmissivity increases.

The next step is to solve for the flow through the network. We do so by imposing constant head boundary conditions such that the global hydraulic head gradient is $\frac{\partial h}{\partial x} = -0.1$ and $\frac{\partial h}{\partial y} = 0$, and therefore the dominant flow direction is from left to right in Fig. 1. Assuming Darcy’s law describes flow within each fracture segment, we then solve for the steady-state head distribution, defined at each fracture intersection according to

$$\nabla^2 h = 0. \tag{1}$$

This assumes that the fracture network is fully saturated with incompressible fluid. From the head distribution, we calculate the flux of fluid through each fracture segment according to Darcy’s law:

$$q = -\frac{T}{b} \nabla h, \tag{2}$$

where T is the fracture transmissivity and b is the fracture aperture. The fracture aperture is related to the transmissivity by way of the cubic law:

$$T = \frac{b^3 \rho g}{12\mu}, \tag{3}$$

where ρ and μ are the density and dynamic viscosity of the fluid (water) and g is gravitational acceleration [3,28]. In combination, these laws assume low Reynolds number flow

through a fracture segment with constant aperture (envisioned as the fracture being bounded by parallel plates).

Finally, we simulate advective transport through the DFNs (dispersion along the length of the fracture and matrix diffusion are not considered). We use a particle tracking method in which the solute mass is discretized into particles of equal mass initially distributed over a 50 m \times 50 m region along the upstream boundary, as shown in Fig. 1. The number of particles injected into each fracture segment is proportional to its flux (q). After particles are released at fracture intersections, each particle then proceeds through a segment at constant velocity:

$$\mathbf{v} = q\hat{\mathbf{u}}, \tag{4}$$

where $\hat{\mathbf{u}}$ is the unit vector parallel to the fracture segment. Once the particle reaches the end of the fracture segment, it chooses a new segment (s_i) with probability proportional to its flux (q_i). That is

$$P(s_i) = \frac{q_i}{\sum_{i=1}^{n_{\text{seg}}} q_i}, \tag{5}$$

where n_{seg} is the number of segments connected to the current segment. This treatment assumes that dispersion along the fracture length is negligible and that the concentration of solute across the fracture width is uniform. Therefore, the method relies on complete mixing at the fracture intersections assuming that the velocity distribution within the fracture network is quickly sampled by the solute compared with the amount of time it spends in the fracture because of the fracture’s low aspect ratio. This assumption has been assessed in both smooth- and rough-walled fractures [29,30]

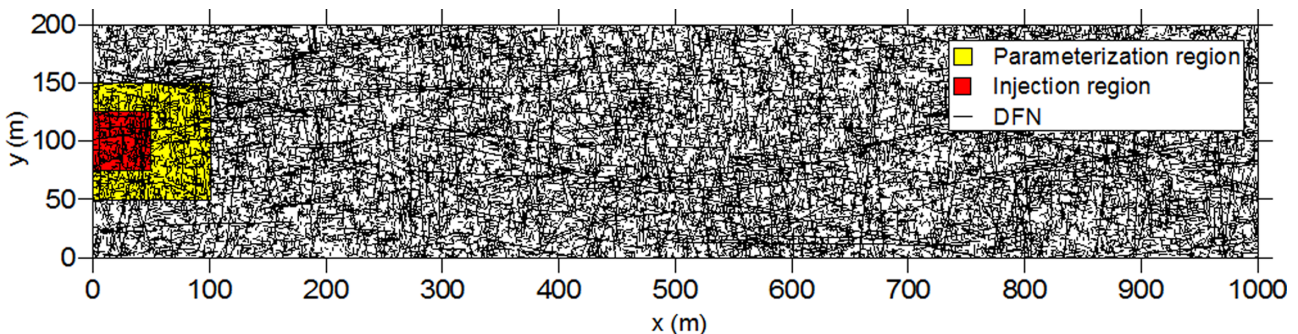


FIG. 1. Modeling domain: one realization of a DFN with injection region highlighted in red and parametrization region highlighted in yellow.

and leads to negligible errors, especially in rough walled fractures. Once the particle reaches the boundary of the DFN, it is removed from the system (all boundaries are absorbing). Each simulation is run until all particles have been removed. This flux-weighted particle-tracking method is distinct from the upscaled models discussed in Sec. III because the particles in this case have access to the full details of the DFN and all segment selections depend on the spatial location of the particles and the flux of the connecting segments.

In addition to simulating transport over the entire DFN, we delineate a small 100 m \times 100 m region along the upstream boundary and run another transport simulation to obtain parameters to use in the upscaled models. The particle trajectories obtained over this smaller region are analyzed and used to create space and time step distributions for the set of upscaled models in Sec. III. For this reason, we refer to this region of the domain as the “parameterization region.” For the full DFN transport simulations, we use 10^5 particles. For the parametrization simulations, we use 10^6 particles so that we have a large number of trajectories to analyze. For visualization purposes, Fig. 1 shows the modeling domain and how it is partitioned into different regions.

B. Effect of transmissivity distribution on fracture fluxes

It can be seen from Eq. (2) that an increase in the range of fracture fluxes occurs as the range of transmissivity increases (flux is proportional to transmissivity). The range of transmissivity is controlled by the standard deviation of the transmissivity distribution (σ). Figure 2 shows the PDF of the absolute value of fracture fluxes, $f_{|q|}(x = |q| \text{ in } \frac{\text{m}}{\text{s}})$, where q_i is the measured flux through segment i , which is obtained from all segments in 50 realizations of each of the three transmissivity distributions. The PDFs are bimodal, with peak values generally decreasing as σ increases, which spreads the PDF out toward high-flux fractures. Bimodality is commonly found in DFN flux distributions (e.g., Refs. [31,32]), which in this case it is likely because there are two fracture sets: one aligned with the pressure gradient and one perpendicular to the pressure gradient (see the parameters of the angle distribution in Table I). This nonmonotonicity is a property that each of the upscaled models must be capable of simulating. Figure 2 also shows the complimentary cumulative distribution function (CCDF) of flux to highlight the tail of the distribution.

In upscaled models, it is more difficult to capture the effect of the transmissivity distribution on the presence of connected high-velocity flow channels or preferential pathways. Figure 3 shows the correlation coefficient between instantaneous particle velocities at various distances along the particle paths. As σ increases, particle velocities become more correlated, at least for distances below 100 m.

In Fig. 2 and in the remainder of this manuscript, all results are derived from a set of 50 realizations of the DFN for each value of σ . The number of realizations generated is chosen by comparing moments of breakthrough curves from each realization to moments of the ensemble breakthrough curve at the furthest distance from the inlet (1 km); details are available in the Appendix.

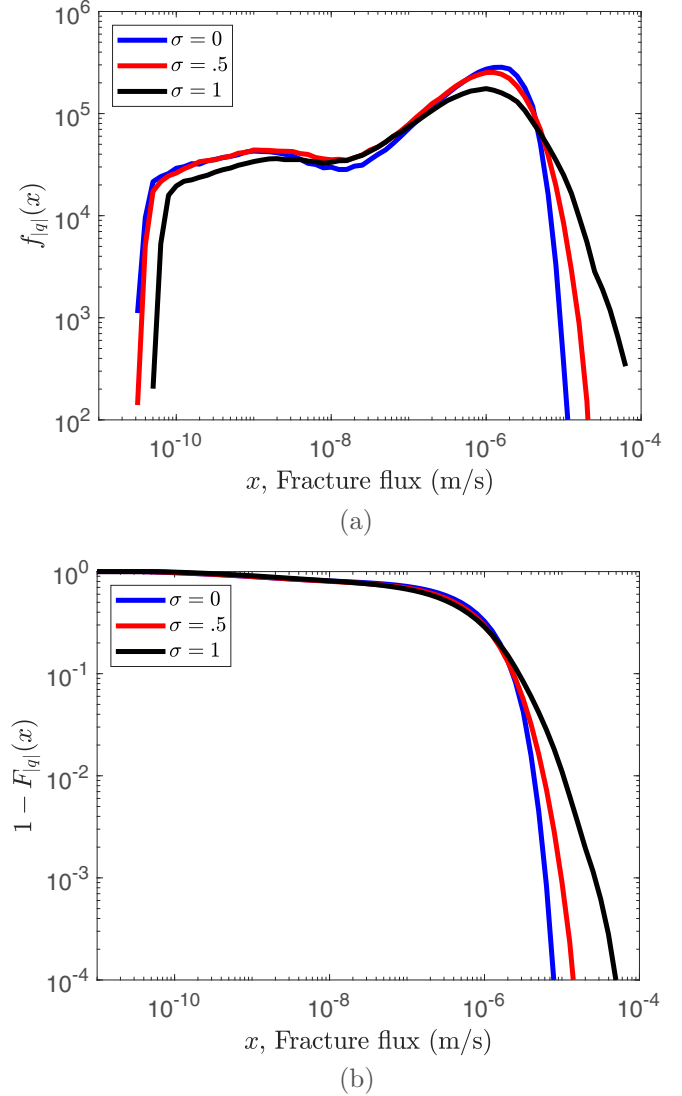


FIG. 2. Fracture flux magnitude for various values of the standard deviation of the transmissivity distribution (σ) (a) PDF [$f_{|q|}(x)$], (b) CCDF [$1 - F_{|q|}(x)$].

III. UPSCALED MODELING

Following the extraction of trajectory data from the small DFN simulations (done over the parametrization region), we use this (numerical) data to create space and time step distributions for the three upscaled random walk models. The goal is to use these models to predict the breakthrough at locations outside of the parametrization region. Although the capability of the upscaled models to match the large scale DFN simulations will be assessed, they do not have access to the statistics of the full DFN, so their results are referred to as predictions. Furthermore, each realization of the upscaled models only has access to the trajectories from the parametrization region of a single realization. In this section, we briefly introduce each of the upscaled random walk models used to predict transport in the DFNs.

Each of the three models considered here can be categorized as a continuous time random walk (CTRW) [12]. In CTRWs, the solute is discretized into particles of equal mass,

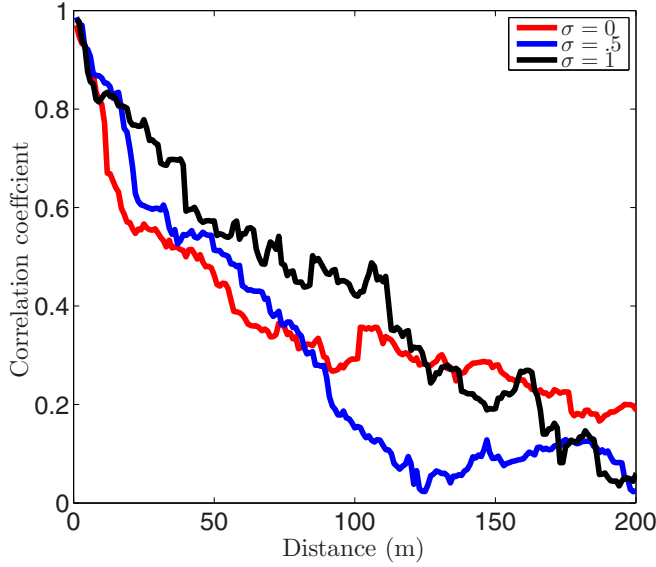


FIG. 3. Spatial correlation between particle velocities measured in DFNs with different transmissivity distributions.

which take steps in space and time, sampled from a density of $f(\delta x, \delta y, \delta t)$, where δx , δy , and δt may or may not be coupled. For fracture networks, usually a step is considered to be the spatial and temporal jump a particle would make through a single fracture segment. However, a variety of step definitions are considered to determine the effect of modeling scale on the accuracy of the predictions. Descriptions of the individual models are discussed later in this section. Once the concept of what constitutes a step is defined, particles are injected into the domain (in the red square in Fig. 1). Each particle then transitions through space and time according to

$$\begin{aligned} x_n &= x_{n-1} + \delta x_n, & y_n &= y_{n-1} + \delta y_n, \\ t_n &= t_{n-1} + \delta t_n, & n &= 1, 2, 3, \dots, \end{aligned} \quad (6)$$

where the random triplet $(\delta x_n, \delta y_n, \delta t_n)$ comes from $f(\delta x, \delta y, \delta t)$ and may or may not depend on $(\delta x_{n-1}, \delta y_{n-1}, \delta t_{n-1})$. Note that there is no requirement that δx , δy , or δt be decoupled or fixed. Most often, $f(\delta x, \delta y, \delta t)$ is a parameterized probability density, which allows for analytical solution of concentration distributions if the space and time steps are uncoupled [33]. Although this is less convenient, the theory allows for more general empirical densities, including coupled space and time steps [34]. The key to the creation of any CTRW model is the parametrization of $f(\delta x, \delta y, \delta t)$, which is assumed to be independent of particle position (i.e., statistically stationary in space).

Generally, steps are taken to be independent and identically distributed, but we consider both correlated and uncorrelated steps. This distinction may affect model predictions, depending on how much correlation exists between successive steps in the DFN simulations [21,35,36], which depends on the geometric and hydraulic attributes of the DFN. In all three of the upscaled random walk models described in this section, each step a particle makes in space and time can depend on its previous step. This correlation between steps is accounted for using a one-step Markov chain to relate the current step

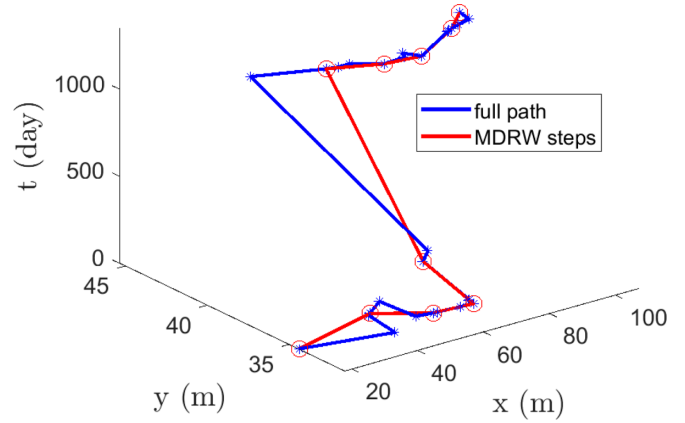


FIG. 4. Method for partitioning particle trajectories into MDRW modeling steps. Stars represent fracture intersections of the original trajectory (in steps of one fracture segment). Circles represent the intersections between two-segment steps.

to the previous step. Continuous time random walk models, without the added complexity of a one-step Markov chain, have been used successfully to describe transport through fracture networks [13,14].

For each realization of all of the upscaled models, we inject 10^5 particles, whose initial distribution matches the initial condition in the DFN simulations (recall the particles are initially distributed over a 50×50 m region along the upstream boundary, where the number of particles that start at each location is weighted by fracture segment flux). We use absorbing boundary conditions to match the boundary conditions in the DFN simulations, which means that particles that move outside of the domain are removed from the simulation. Each simulation is run until all particles have been removed.

A. Markov directed random walk (MDRW)

The MDRW model was introduced in Ref. [10]. In addition to modeling correlation between steps with a Markov chain, it also provides further flexibility to explicitly model retention, a feature which we do not require because our DFN simulations are not designed to model retention.

We define the steps $(\delta x_n, \delta y_n, \delta t_n)$ to correspond to transport through a fixed number of fracture segments, k . This is done by splitting every trajectory from our parametrization simulations into groups of k segments and recording the distance and travel time from the beginning of the first segment in each group to the end of the k th segment in each group. Therefore, from each trajectory, depending on the number of segments it passes through, we are often able to extract multiple samples that can be used to construct $f(\delta x_n, \delta y_n, \delta t_n)$. Figure 4 shows the full path of an individual particle and how it is partitioned into steps of length $k = 2$. Larger values of k would produce larger values of the triplet $(\delta x_n, \delta y_n, \delta t_n)$ and smoother trajectories.

To account for correlation between steps, we first define a set of 20 discrete equiprobable states based on speed. Each state is defined by a range of speed, which for state s_i is from l_{i-1} to l_i , where $l_0 \equiv 0$. A particle is in state s_i at step n if its speed, q_n , is between l_{i-1} and l_i . The speed of each step is

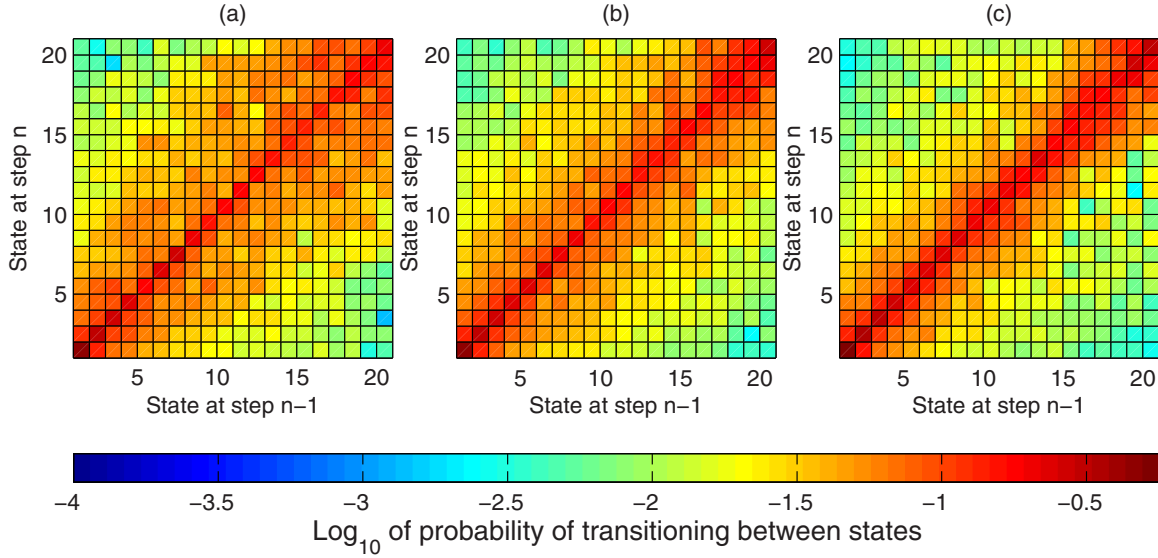


FIG. 5. Ensemble averaged transition matrix $[P(q_n \in s_i | q_{n-1} \in s_j)]$ over all realizations with modeling step size $k = 1$ fracture segments for transmissivity distributions with (a) $\sigma = 0$, (b) $\sigma = 0.5$, and (c) $\sigma = 1$.

defined by

$$q_n = \frac{\sqrt{\delta x_n^2 + \delta y_n^2}}{\delta t_n}. \quad (7)$$

This means that low-numbered states cover low speeds and high-numbered states cover high speeds.

Given this definition, we can create a Markov chain, which consists of the initial (now discretized) distribution and a transition matrix using the trajectories from the DFN simulations. The transition matrix is the conditional probability that the speed at step n is in state s_i given that the speed at step $n - 1$ is in state s_j , $P(q_n \in s_i | q_{n-1} \in s_j)$. Figure 5 shows the transition matrix, $P(q_n \in s_i | q_{n-1} \in s_j)$, averaged over all 50 realizations for each transmissivity distribution, using a single fracture segment ($k = 1$) as the modeling step. This is obtained by creating transition matrices for each realization, adding them together, and then dividing by the number of realizations. All of the transition matrices are diagonally dominant, which indicates a tendency for particles to remain in their current speed state. We attribute this behavior to preferential pathways that form because of the connectivity of high-flux fractures (e.g., see Refs. [37–40]). As the spread of the transmissivity distribution increases with σ , the probability of particles transitioning many states in one step decreases, which can be seen in the slandering of the bands around the diagonal. This indicates that the correlation between a particle's speeds does increase with increasing σ (as also evidenced in Fig. 3 at scales less than 100 m). Note that an MDRW model, which uses only one speed state, would automatically have uncorrelated steps. Therefore, the construction of the MDRW (and the other two models discussed hereafter) allows us to run simulations in both correlated and uncorrelated forms and compare their performance.

This is all the information necessary to run the MDRW simulations. Each particle transitions through space and time

according to Eq. (6), with

$$f_{MDRW}(\delta x, \delta y, \delta t) = f(\delta x_n, \delta y_n, \delta t_n | q_n \in s_i) \times P(q_n \in s_i | q_{n-1} \in s_j). \quad (8)$$

This model has been successfully applied to transport through DFNs in Ref. [10], which gives further details of the model.

B. Monte Carlo solution of the Boltzmann transport equation (BTE)

The BTE model was introduced in Ref. [16]. It also models correlation between steps with a Markov chain, but based on velocity (both speed and direction). It defines steps $(\delta x_n, \delta y_n, \delta t_n)$ to correspond to transport through a fixed number of fracture segments, k , so DFN particle trajectories are split up in the same way as with the MDRW. Contrary to the MDRW methodology, the step length of a particle as it travels at the velocity sampled from the DFN trajectories is also random (albeit dependent on velocity state) rather than being the same length as the corresponding trajectory segment.

To do this, spatial steps are put in polar form:

$$\delta x_n = d_n \cos \theta_n, \quad \delta y_n = d_n \sin \theta_n, \quad (9)$$

where d_n is log uniformly distributed between limits that depend on the velocity class and θ_n is the angle of the randomly chosen trajectory.

To account for correlation between steps, and to define the distribution of d_n , we first define a set of 10 discrete equiprobable states based on speed. Similar to MDRW, each state is defined by a range of speeds, which for state s_p is l_{p-1} to l_p , where $l_0 \equiv 0$. From here, we find the average jump length of trajectory segments corresponding to each state, which for state s_p is \bar{r}_p . The distance a particle travels at its current

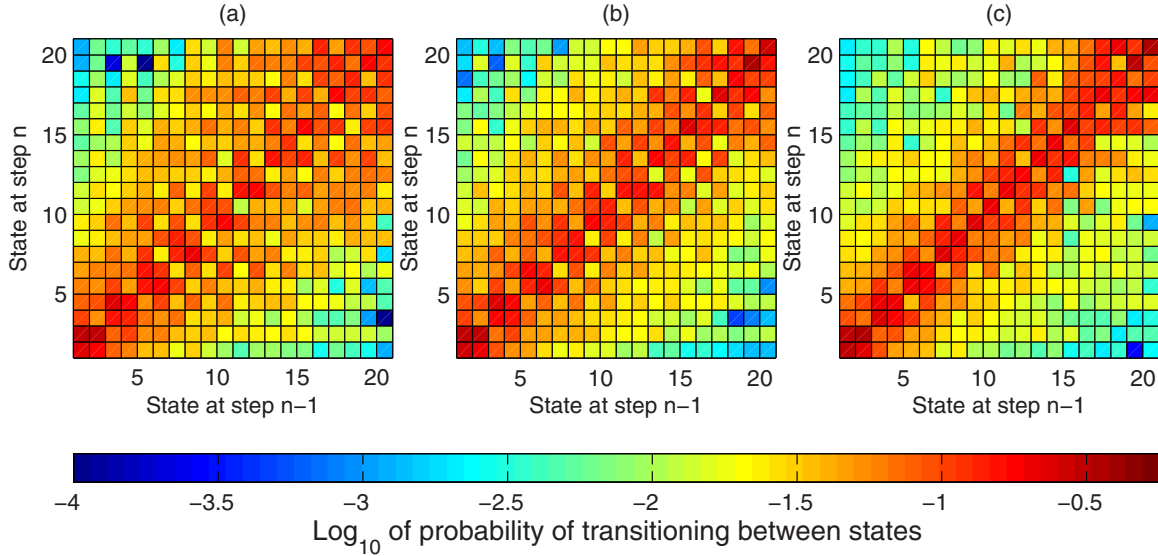


FIG. 6. Ensemble averaged transition matrix ($P[(q_n, \theta_n) \in s_i | (q_{n-1}, \theta_{n-1}) \in s_j]$) over all realizations with modeling step size $k = 1$ fracture segments for transmissivity distributions with (a) $\sigma = 0$, (b) $\sigma = 0.5$, and (c) $\sigma = 1$.

velocity, d_n , is then generated as

$$d_n = -\ln(U)\bar{r}_p, \quad (10)$$

where U is a uniform random number between 0 and 1. Therefore, in theory, a particle may continue at its current velocity until it travels a distance between 0 and ∞ times the length of the trajectory segment.

Next, the distribution of speed states is further discretized by angle to create velocity states. For our purposes, because we want the BTE to have the same number of states as the MDRW, we split each speed state into two equiprobable angle bins (for a total of 10 speed \times 2 angles = 20 velocity states). The full range of possible angles is $[-\pi, \pi]$, with an angle of 0 being aligned with the predominant flow direction. Because we are only using two angle states for each speed bin, we split the absolute value of the angles into “upstream” $[0, \pi/2]$ and “downstream” $(\pi/2, \pi]$. A particle is in velocity state $s_{i=2(p-1)+q}$ if its speed is in state s_p and the absolute value of its angle is between angle limits $l_{p,q-1}$ to $l_{p,q}$, where $l_{p,0} \equiv 0$, which are defined for each speed state p separately. Although the distribution of angles can be further discretized, the number of bins here is kept minimal for the sake of simplicity and comparison with the other models.

Given this definition, we then approximate the transition matrix, which is the conditional probability $P[(q_n, \theta_n) \in s_i | (q_{n-1}, \theta_{n-1}) \in s_j]$, using the trajectories from the DFN simulations. Figure 6 shows the transition matrix averaged over all realizations for each transmissivity distribution, using a single fracture segment ($k = 1$) as the modeling step. As with speeds (Fig. 5), as σ increases, the correlation between successive velocities also increases, although the bandwidth of the transition matrices for velocities is larger than the transition matrices for speeds. As with the MDRW, a BTE model that uses only one velocity state would have uncorrelated steps, so we can also run the BTE in both correlated and uncorrelated forms and compare them.

Each particle transitions through space and time according to Eq. (6), with

$$f_{\text{BTE}}(\delta x, \delta y, \delta t) = f[d_n \cos \theta_n, d_n \sin \theta_n, \delta t_n | (q_n, \theta_n) \in s_i],$$

$$P[(q_n, \theta_n) \in s_i | (q_{n-1}, \theta_{n-1}) \in s_j]. \quad (11)$$

This model has been successfully applied to transport through DFNs in Ref. [16], which gives further details of the model.

C. Spatial Markov model (SMM)

The SMM model was introduced in Ref. [15]. It also models correlation between steps with a Markov chain, but based on speed over fixed longitudinal spatial increments of length L . It defines steps $(\delta x_n = L, \delta y_n, \delta t_n)$ to correspond to transport over increments of length L in the longitudinal direction. In a sense, this means that we are projecting onto the axis longitudinal to transport the correlations between velocities at different spatial locations and implicitly assuming these are the dominant correlations in the DFN. This inherently assumes incremental stationarity for the correlations, as the same transition matrix is expected to be valid along the entire SMM path [41]. To keep the average modeling scale the same for all models, we set $L = L_k$ to be the average longitudinal step taken by particles over k fracture segments, defined as

$$L_k = \frac{1}{N} \sum_{i=1}^N r_i \cos \theta_i, \quad (12)$$

where r_i and θ_i are the length and angle of trajectory i over k segments, and N is the number of trajectories. For $k = 1, 2, 3$ fracture segments, $L_k \approx 3, 5, 7$ m, respectively. The trajectories from the DFN simulations are then used to create breakthrough curves along the longitudinal direction of the parametrization region at increments of length, L_k (e.g., for $k = 2$, we create 20 breakthrough curves, each at 5 m increments). Then, for each location, X , we find the distribution of travel times, $f_t(X, t)$, using Eq. (15).

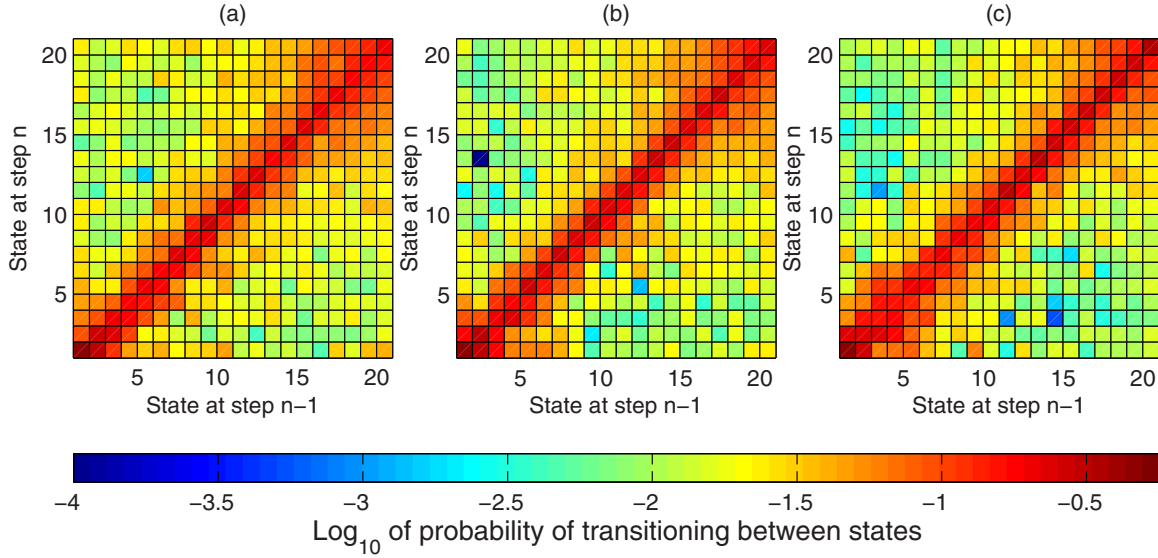


FIG. 7. Ensemble averaged transition matrix $[P(\delta t_n \in s_i | \delta t_{n-1} \in s_j)]$ over all realizations with modeling step size $L_{k=1}$ (the average length of 1 fracture segment) for transmissivity distributions with (a) $\sigma = 0$, (b) $\sigma = 0.5$, and (c) $\sigma = 1$.

To account for correlation between steps, we first define a set of 20 discrete equiprobable states based on travel times. Because L_k is fixed, this is equivalent to defining states based on speed, as in the MDRW. Each state is defined by a travel-time range, which for state s_i is l_{i-1} to l_i , where $l_0 \equiv 0$. We then approximate the transition matrix, which is the conditional probability $P(\delta t_n \in s_i | \delta t_{n-1} \in s_j)$, using the trajectories from the DFN simulations. Figure 7 shows the transition matrix averaged over all realizations for each transmissivity distribution. As with speeds (Fig. 5) and velocities (Fig. 6), as σ increases, the correlation between successive travel times also increases. The bandwidth of the SMM transition matrices is wider than that of the MDRW transition matrices, but smaller than that of the BTE transition matrices. As with both the MDRW and the BTE models, an SMM model that uses only one travel-time state would have uncorrelated steps, so we can also run the SMM in both correlated and uncorrelated forms and compare them.

Each particle transitions through space and time according to Eq. (6), with

$$f_{\text{SMM}}(\delta x, \delta y, \delta t) = \delta(L - \delta x_n) f(\delta y_n, \delta t_n | \delta t_n \in s_i) \times P(\delta t_n \in s_i | \delta t_{n-1} \in s_j). \quad (13)$$

Versions of this model has been successfully applied to transport through DFNs [17,42], even in real fractured rock [43]. Further details of the model are provided in Ref. [15].

D. Importance of correlation of each model

To further quantify the importance of correlation in these models and to account for variability between realizations, we looked at the importance of correlation parameter (IC), originally introduced in Ref. [35]. The importance of correlation

parameter is defined as

$$\text{IC} = \frac{1}{N} \sum_{i=1}^N \sum_{j=1}^N T_{ij}^2, \quad (14)$$

where N is the number of states in transition matrix T_{ij} . This metric ranges from $\frac{1}{N}$, for a completely uniform transition matrix (no correlation), to 1 for a diagonal of ones, with every other entry being zero (perfect correlation). Figure 8 shows boxplots of IC for each transmissivity distribution. In all cases, the BTE model has the most variability in IC, followed by MDRW, with SMM having the least variability. For all three models, the median IC increases with σ , indicating that correlation is increasingly important as transmissivity becomes more heterogeneous.

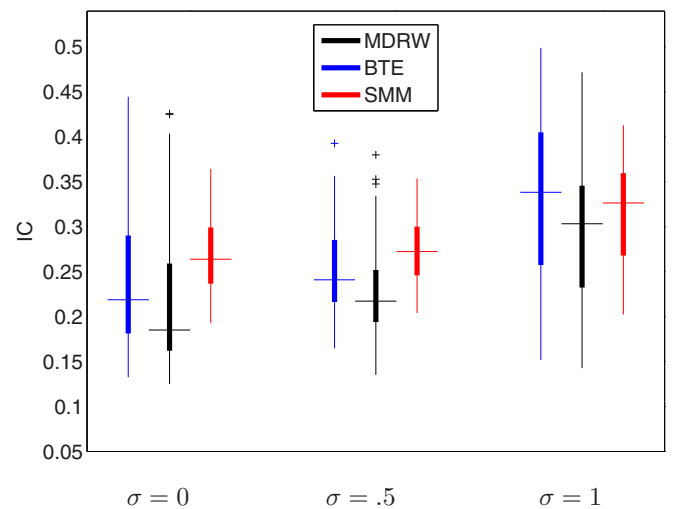


FIG. 8. Boxplots of the importance of correlation parameter for transmissivity distributions with different values of σ . Plus signs indicate outliers.

All three upscaled random walk models are quite similar because they all rely on Markov chains. The states of the Markov chains differ between models, from the simplest model, which relies on longitudinal flux (SMM), to total flux (MDRW), to the most complicated model, which relies on full velocity (BTE). Intercomparison between models allows us to determine the extent of the velocity information required to properly account for correlation, whereas model intracomparison allows us to determine whether correlation needs to be accounted for at all. The challenge with all of the models is ensuring sufficient parametrization. The amount of data needed for sufficient parametrization is reduced for the uncorrelated versions of the models because the transition matrices required for correlated models are based on more information than just the distribution $f(\delta x, \delta y, \delta t)$.

IV. RESULTS

Here, we compare the breakthrough results of the upscaled random walk models to the large-scale DFN simulations. We focus largely on ensemble statistics created using aggregates of particles in all realizations. Each upscaled model is run using three different modeling scales, for which the number of fracture segments used to define a step are $k = 1, 2, 3$. Furthermore, we run each model in both correlated and uncorrelated forms. Recall that the uncorrelated forms differ from the correlated forms in that their corresponding Markov chains consist of a single state. These uncorrelated models are referred to as uMDRW, uBTE, and uSMM.

A breakthrough curve at location X is a measure of concentration arriving at that location, which is related to the distribution of times it takes particles to arrive at the location by

$$f_\tau(X, t) = \int_{-\infty}^{\infty} \frac{C(x = X, y, t)}{C_{\text{tot}}(X)} dy, \quad (15)$$

where $f_\tau(X, t)$ is the probability of a particle arriving at location X at time t , $C(x = X, y, t)$ is the concentration of solute arriving at location X, y at time t , and $C_{\text{tot}}(X)$ is a normalization constant, which is the integral of $C(x = X, y, t)$ over all time. Note that constant head boundary conditions are assigned in the transverse direction (as opposed to no-flow boundary conditions), and therefore C_{tot} is not equal to the amount of concentration initially injected because particles are free to exit the DFN through the transverse boundaries.

The metrics we use to test the predictive capability of each upscaled model are:

(1) Relative mean absolute error in the ensemble cumulative travel-time distributions, $F_\tau(X, t)$ at $X = 500$ m and $X = 1$ km.

(2) Relative mean absolute error in total mass in ensemble breakthrough curves, $C_{\text{tot}}(X)$, at ten intervals of 100 m length along the entire domain ($X = 100, 200, \dots, 900, 1000$ m).

To calculate the relative mean absolute error in $F_\tau(X, t)$, we discretize time into one-hundred-day increments up to the longest travel time from the DFN simulations. The error is

then defined as

$$\text{rMAE}[F_{\tau, \text{mod}}(X)] = \frac{\sum_{i=1}^n |F_{\tau, \text{DFN}}(X, t_i) - F_{\tau, \text{mod}}(X, t_i)|}{\sum_{i=1}^n F_{\tau, \text{DFN}}(X, t_i)}, \quad (16)$$

where $F_{\tau, \text{DFN}}(X, t_i)$ and $F_{\tau, \text{mod}}(X, t_i)$ are the cumulative travel-time distributions at time t_i for the DFN and upscaled model simulations, respectively.

The relative mean absolute error in $C_{\text{tot}}(X)$ is defined as

$$\text{rMAE}(C_{\text{tot}}) = \frac{\sum_{i=1}^{10} |C_{\text{tot,DFN}}(X_i) - C_{\text{tot,mod}}(X_i)|}{\sum_{i=1}^{10} C_{\text{tot,DFN}}(X_i)}, \quad (17)$$

where $C_{\text{tot,DFN}}(X_i)$ and $C_{\text{tot,mod}}(X_i)$ are the total mass in the breakthrough curves at location X_i for the DFN and upscaled model simulations, respectively.

These metrics are used so that errors in prediction of longitudinal and transverse transport are kept separate. The errors in the cumulative travel-time distribution tell us how well the models are predicting longitudinal transport, whereas the total mass in the breakthrough curves tells how well the models are predicting transverse transport because any mass not contained in the breakthrough curve has escaped the domain through a transverse boundary. Because of the boundary conditions and the high aspect ratio of the domain, we find C_{tot} to be a better measure of transverse behavior than spatial moments.

A. Longitudinal predictions: Error in the ensemble cumulative travel-time distributions

Figure 9 shows the cumulative and complementary cumulative travel-time distributions at $x = 500$ m of DFN simulations with each transmissivity distribution ($\sigma = 0, 0.5, 1$) and of upscaled random walk model simulations with modeling step $k = 1$, along with the corresponding error. By looking at the cumulative distribution function (CDF) on a log-log scale, we can zoom in on how well each model is capturing the pre-peak portion of the breakthrough curve. For $\sigma = 0$ [Fig. 9(a)], the SMM predicts too much early breakthrough and the uBTE predicts too little, which means that fast particles are too fast in the SMM model and too slow in the uBTE model. The predictions of the other models are nearly identical and are close to the ensemble DFN result. By looking at the CCDF on the same scale, we can zoom in on how well each model is capturing the tail of the breakthrough curve. The uSMM and SMM capture the tail of the DFN breakthrough well, but all other models predict too much late breakthrough, which means that the slow particles in these models are too slow. For $\sigma = 0.5$ [Fig. 9(b)], the CDF shows that the MDRW and BTE overpredict early breakthrough almost as much as the SMM does. The predictive capability of each model on the tailing behavior is largely unchanged with changing σ . For $\sigma = 0.5$, correlation is negligible (which can also be seen in Fig. 8) and accounting for correlation in this situation leads to increased error. This could possibly be because the numerical error in the calculation of the transition matrices is of the same order as the small amount of correlation that actually exists, particularly at early times. For $\sigma = 1$ [Fig. 9(c)], the CDF shows that the uncorrelated models severely underpre-

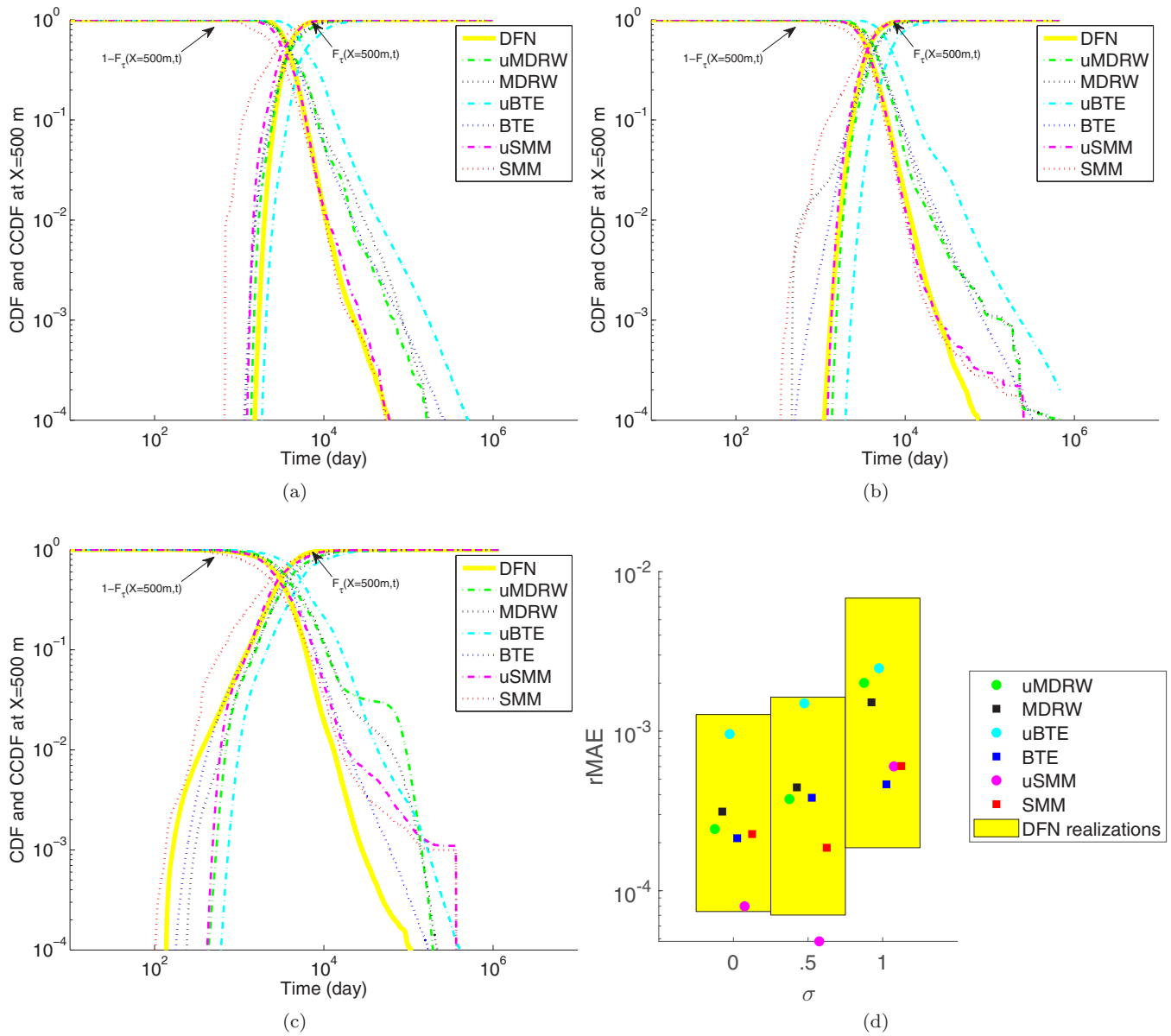


FIG. 9. Ensemble cumulative and complementary cumulative travel-time distributions at $x = 500$ m of large-scale DFN simulations and of upscaled random walk model simulations with modeling step size $k = 1$ with transmissivity distributions (a) $\sigma = 0$, (b) $\sigma = 0.5$, and (c) $\sigma = 1$ and (d) the corresponding relative error. The shaded yellow region shows the range of errors among individual DFN realizations.

dict the early breakthrough, whereas the correlated models come closer to capturing the true DFN behavior. This indicates that for $\sigma = 1$, correlation is important and accounting for it leads to a reduction in error. In this case the BTE model best predicts the tailing behavior. Both SMM models begin to predict the tailing behavior well, but deviate from the DFN result at very long times (over 10^5 days), which is likely because the transport process is projected onto the longitudinal axis for the SMM. With the significant difference in early breakthrough predictions, the correlated models edge out their uncorrelated counterparts in relative error as shown in Fig. 9(d). The only model that predicts both the early and late breakthrough well is the uSMM, which has the lowest relative error. The only model that predicts both poorly was the uBTE, which has the highest relative error. The errors of the other models fall between these two models. To fur-

ther illustrate the tailing behavior of the upscaled models, Appendix B shows the mean-squared logarithmic error of the complimentary cumulative travel-time distributions.

Figure 9(d) also shows the range of errors of each individual realization of the DFN simulations (yellow boxes). Note that these are not typical error bars, because the error in the ensemble prediction can be below the yellow boxes (in fact, the ensemble error of the DFN simulations is by definition 0, whereas the realization error range, shown in yellow, is not). The ensemble predictions for all models are within the range of error of individual DFN simulations. This means that the error in ensemble upscaled models is within the range of error because of the variability of the individual DFN realizations. For those interested in the amount of variability between individual DFN realizations, Appendix C shows the cumulative and complementary cumu-

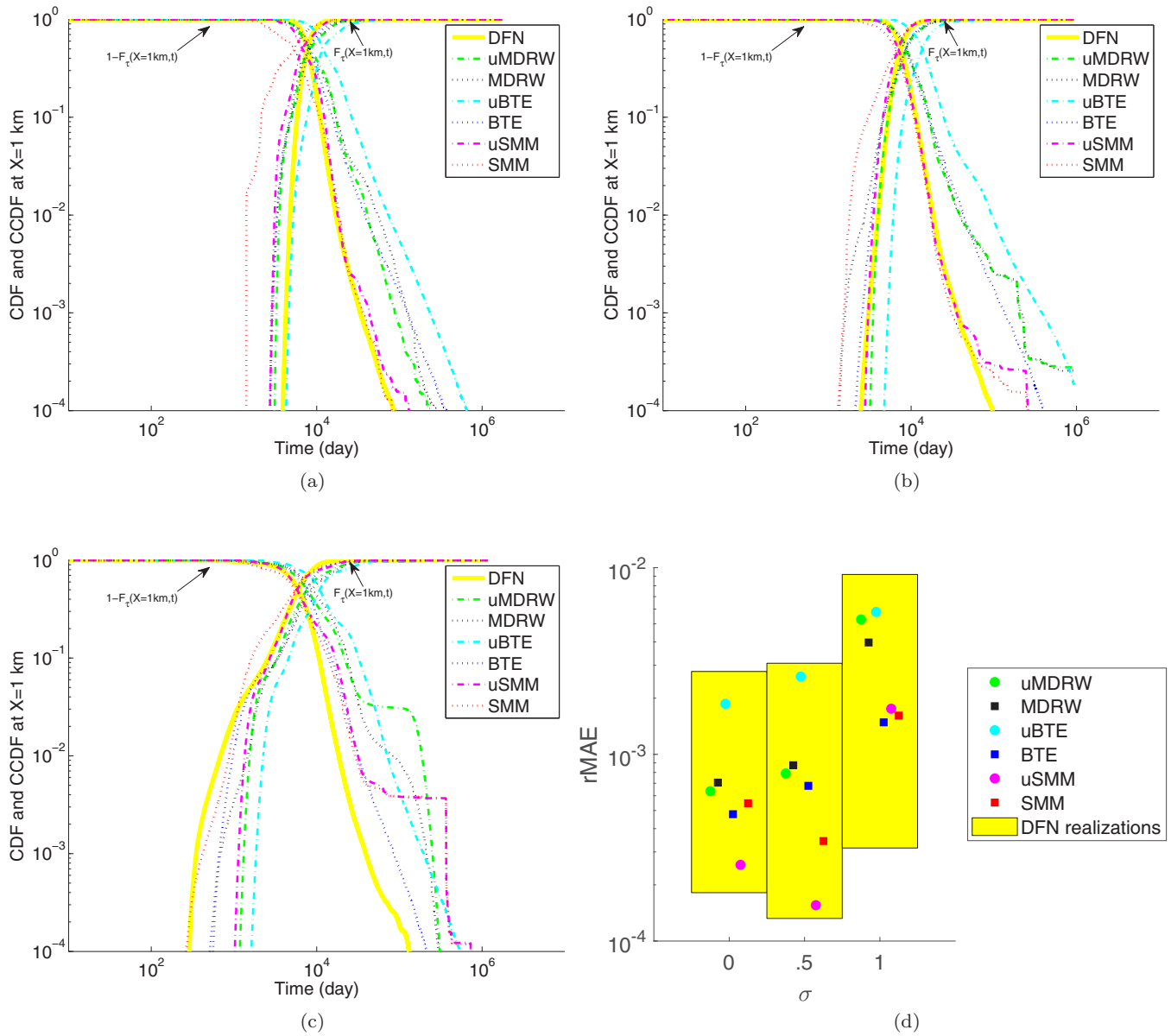


FIG. 10. Ensemble cumulative and complementary cumulative travel-time distributions at $x = 1$ km of large-scale DFN simulations and of upscaled random walk model simulations with modeling step size $k = 1$ with transmissivity distributions (a) $\sigma = 0$, (b) $\sigma = 0.5$, (c) $\sigma = 1$, and (d) the corresponding relative error. The shaded yellow region shows the range of errors among individual DFN realizations.

lative travel-time distributions of each of the individual DFN realizations.

Figure 10 shows the cumulative and complimentary cumulative travel-time distributions at $X = 1$ km. Qualitatively, the performance of the models continue in the same way as shown in Fig. 9, so model comparability does not change when considering the breakthrough curve further downstream. Note that the early breakthrough behavior of BTE model for $\sigma = 0.5$ begins to improve, as shown in Fig. 10(b), but this change does not strongly affect the overall relative error, shown in Fig. 10(d).

B. Transverse predictions: Error in total mass in ensemble breakthrough curves

Here we compare the total mass in the ensemble breakthrough curves [$C_{tot}(X)$], which is a measure of how many

particles remain in the domain long enough to arrive at the breakthrough location (X). Figure 11 shows the total mass in each ensemble breakthrough curve, taken at 100 m increments, for each fracture transmissivity distribution ($\sigma = 0, 0.5, 1$) and the corresponding error [calculated using Eq. (17)]. Similar to the results shown for longitudinal predictions, the predictions here are also made using a single fracture segment ($k = 1$). The mass is calculated by setting the initial injected concentration, $C_0 = 1$, so that if all particles arrive at the breakthrough location at some time, then $C_{tot} = 1$. For $\sigma = 0$ [Fig. 11(a)], at the first breakthrough location ($X = 100$ m), all model predictions come close to the total mass in the breakthrough curves of the DFN simulations, but at further distances, most of the models begin to underpredict the total mass. This means that most of the models predict an overly high degree of spreading in the transverse direction.

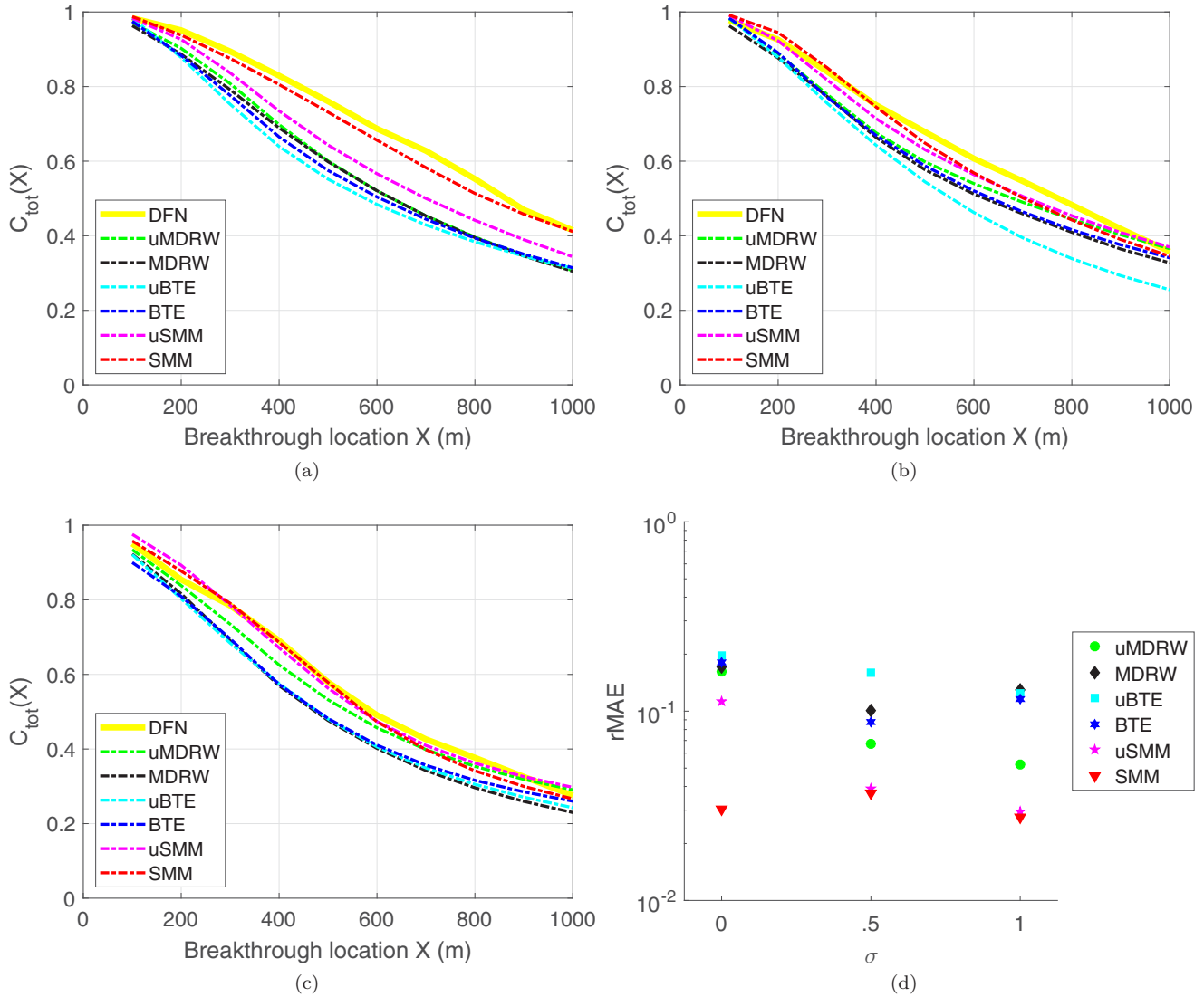


FIG. 11. Total mass in ensemble breakthrough curves of DFN simulations and of upscaled random walk model simulations with modeling step size $k = 1$ with transmissivity distributions (a) $\sigma = 0$, (b) $\sigma = 0.5$, (c) $\sigma = 1$, and (d) the corresponding average relative error.

The SMM outperforms all of the models at all breakthrough locations, followed by the uSMM. As the spread of fracture transmissivity increases, from Figs. 11(a)–11(c), the total mass predictions of the uSMM and uMDRW improve and the results of the uSMM become similar to those of the SMM. Therefore, it can be argued that although the design of the upscaling models tends to overpredict the transverse spread, the difference in DFN-simulated transverse spread and the random-walk-model-produced transverse spread reduces as the heterogeneity in hydraulic properties (i.e., transmissivity distribution) increases. The error in Fig. 11(d) also shows these trends. The similar performance of the MDRW and BTE models in predicting the transverse spreading is probably because the definition of what constitutes a step in these two models is linked to random walk steps over a fixed number of actual fracture segments. Surprisingly, the model which treats transverse behavior in the most trivial fashion (the SMM that takes δy from the transverse jump over fixed longitudinal steps rather than from actual fracture segment geometry) is the one that best predicts transverse behavior, although this may be

due to the aspect ratio of the modeling domain. Overall, it is interesting to observe here that random walk upscaling models are suited to better capture the transverse spread of fracture networks with enhanced hydraulic heterogeneity. This has strong significance for modeling transport in fracture networks because the performance of model evaluation metrics is generally expected to decrease as the complexity of a system increases (as seen in the CDF, CCDF, and error plots of Figs. 9 and 10).

C. Effect of changing modeling scale

Figure 12 shows how the model predictions change as the modeling scale increases from $k = 1$ to $k = 3$ fracture segments for simulations with constant transmissivity distribution ($\sigma = 0$). Although the errors in longitudinal predictions (breakthrough) [Fig. 12(a)] tend to decrease with a larger modeling scale, the transverse behavior of each model [Fig. 12(b)] is not significantly changed by varying the modeling scale over this range, which can be seen in the relatively

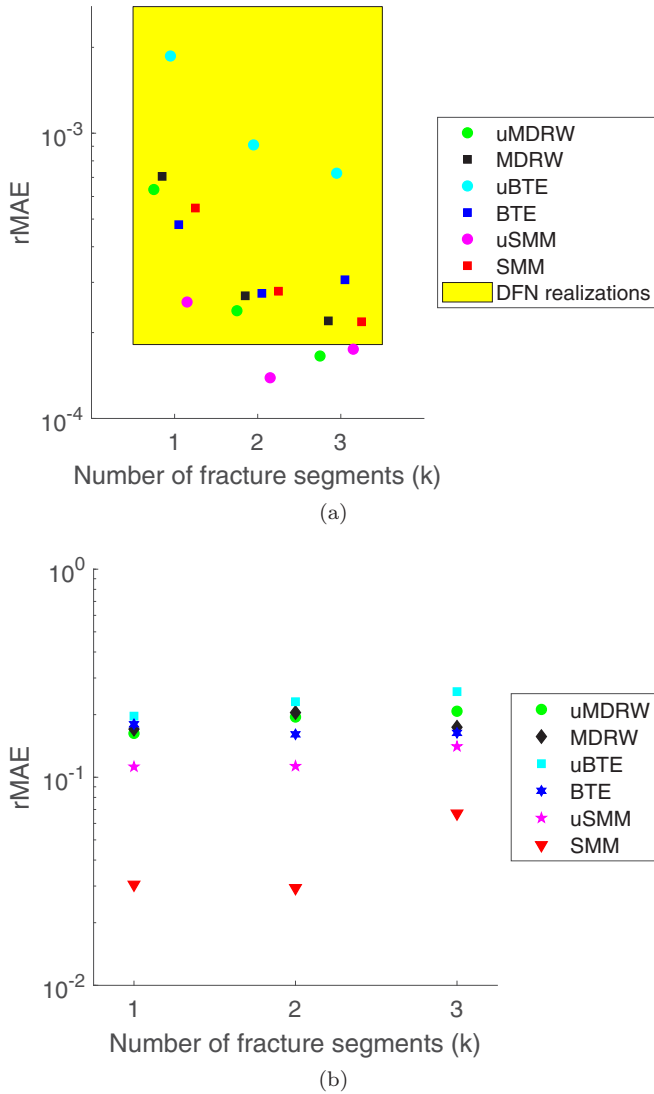


FIG. 12. Relative errors in ensemble upscaled random walk model simulations as a function of modeling scale for $\sigma = 0$: (a) relative error in cumulative breakthrough at $X = 1$ km and (b) average relative error in mass.

constant errors of each model as k increases. This trend exists for all three values of σ . The decreased error in longitudinal predictions for large values of k is understandable because the models are based on data captured from longer continuous portions of particle trajectories. The fact that increasing k does not significantly improve transverse errors is likely due to the combination of the models overpredicting spreading and the aspect ratio of the domain. If we allowed particles to reenter the domain rather than using absorbing boundaries for the upscaled models, then the transverse errors would be reduced overall and we may begin to see improvements with increasing k .

V. DISCUSSION

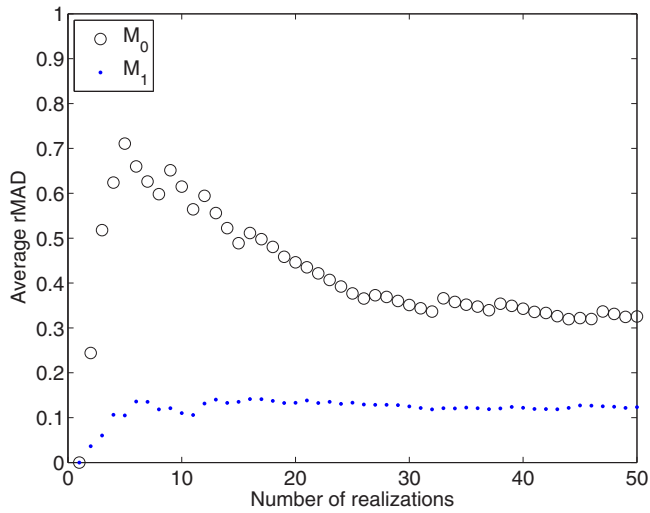
All of the upscaled random walk models can predict the ensemble DFN breakthrough as well as a single DFN realization (recall the yellow boxes in the error plots show the range of

errors in individual DFN realizations). The model predictions differ, so the best model to use depends on what behavior the model is meant to capture. The model comparisons in this manuscript use particles that represent conservative solute, but if the solute to be modeled is nonconservative and degrades over time, it is most important that the model predicts early breakthrough. The models that predict early breakthrough the best were uSMM and uMDRW for $\sigma < 1$ and SMM and BTE for $\sigma = 1$. Alternatively, if the solute is a contaminant and modeling of pump and treat remediation is desired, then it is important that the model effectively predicts the breakthrough curve tail. The models that predict late breakthrough the best are uSMM and SMM for $\sigma < 1$ and MDRW and BTE for $\sigma = 1$. In both of these cases, the best model depends on the fracture transmissivity distribution. If there are no-flow boundary conditions on the transverse sides of the domain, then the error in total mass can be ignored. Otherwise, using SMM for all values of σ , or uSMM for $\sigma > 0$, will better capture the transverse spreading.

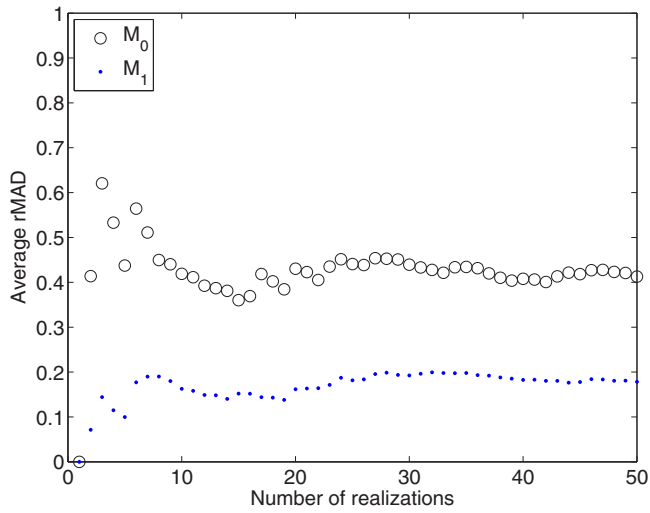
VI. CONCLUSIONS

In this work we focus on the comparison between Lagrangian random walk models, each of which uses particle trajectories from the DFN simulations to create empirical space and time step distributions that are sampled from in the random walk simulations. The three models we focus on are the Markov directed random walk (MDRW) [10], Monte Carlo solution of the Boltzmann transport equation (BTE) [16], and the spatial Markov model (SMM) [15]. We vary and compare multiple scenarios with different fracture transmissivity distributions (with $\sigma = 0, 0.5, 1$) and find the following overall conclusions:

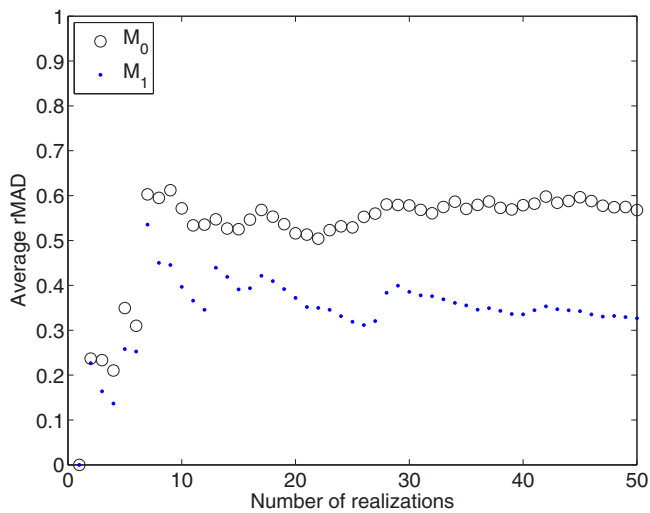
- (1) All models, both correlated and uncorrelated versions, have error within the range of error for single DFN realizations. Therefore, none of the models sacrifice accuracy in exchange for computational cost. The computational time associated with simulating the parametrization region is $\sim 0.8\%$ of the time associated with the full DFN and simulations of multiple parametrization regions can be run in parallel.
- (2) As the distribution of fracture transmissivity widens, preferential pathways for solute form, creating correlation in particle velocities over successive steps.
- (3) For the log-normal transmissivity distributions used here, models that take correlation into account gain an advantage over their uncorrelated counterparts for higher values of σ .
- (4) Early breakthrough is best predicted by the uncorrelated models (uMDRW and uSMM) for $\sigma < 1$ and by the correlated models (BTE and SMM) for $\sigma = 1$.
- (5) Tailing behavior is best predicted by the SMM models (uSMM, SMM) for $\sigma < 1$ and by the correlated BTE and MDRW models for $\sigma = 1$.
- (6) For fracture networks with wide transmissivity distributions ($\sigma = 1$ in this study), the BTE model consistently performs well in predicting both early and late breakthrough.
- (7) Transverse spreading is best predicted by the SMM for all values of σ , and the uSMM for $\sigma > 0$.



(a)



(b)



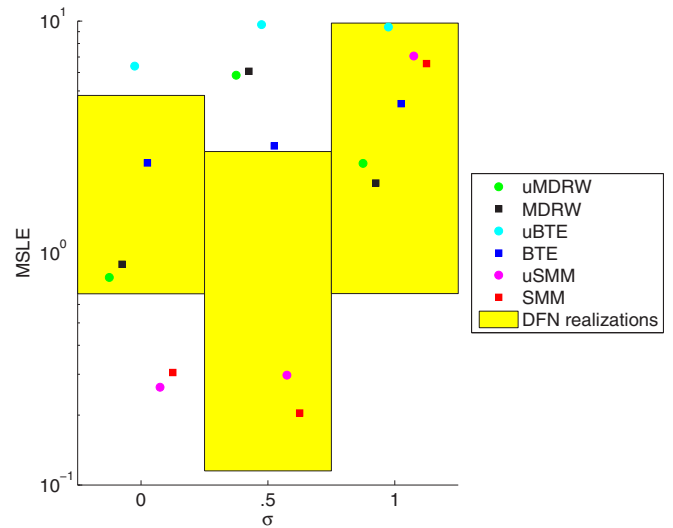
(c)

FIG. 13. Relative mean absolute deviation between moments of breakthrough curves for each realization and moments of the ensemble breakthrough curve, averaged over the number of realizations, for (a) $\sigma = 0$, (b) $\sigma = 0.5$, and (c) $\sigma = 1$.

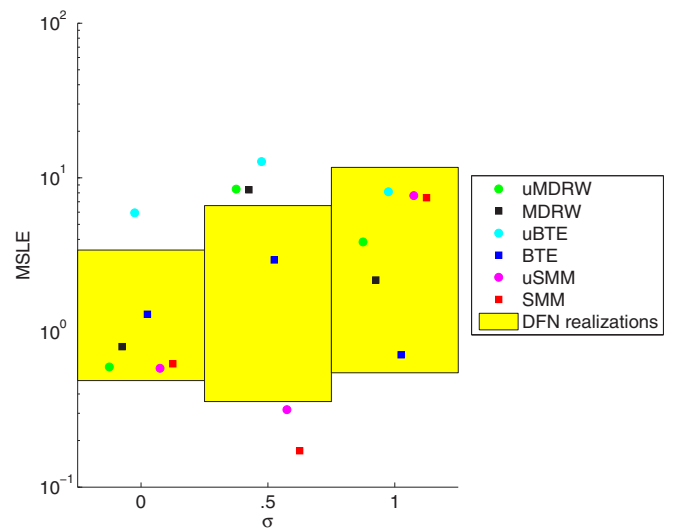
(8) The upscaled random walk models tend to better capture the transverse spreading of DFN simulations for networks with wide transmissivity distributions.

(9) In comparison to the effects of model choice and correlation, the effect of modeling scale (number of fracture segments used to define modeling steps) on model predictive performance is small, at least over the range of $k = 1$ to $k = 3$ covered in this paper.

The results of this study can be used to guide upscaled model selection in fracture network settings. For each DFN realization, we run upscaled simulations for six different models at three different scale lengths for a total of 18 simulations per realization. Through this process, we had hoped we could eliminate some of the models and length scales before moving on to vary other DFN parameters, such as density, fracture length, and angle distributions. The uBTE gives predictions



(a)



(b)

FIG. 14. Mean-squared logarithmic error of complimentary cumulative travel-time distributions of each upscaled model for (a) $x = 500$ m and (b) $x = 1$ km.

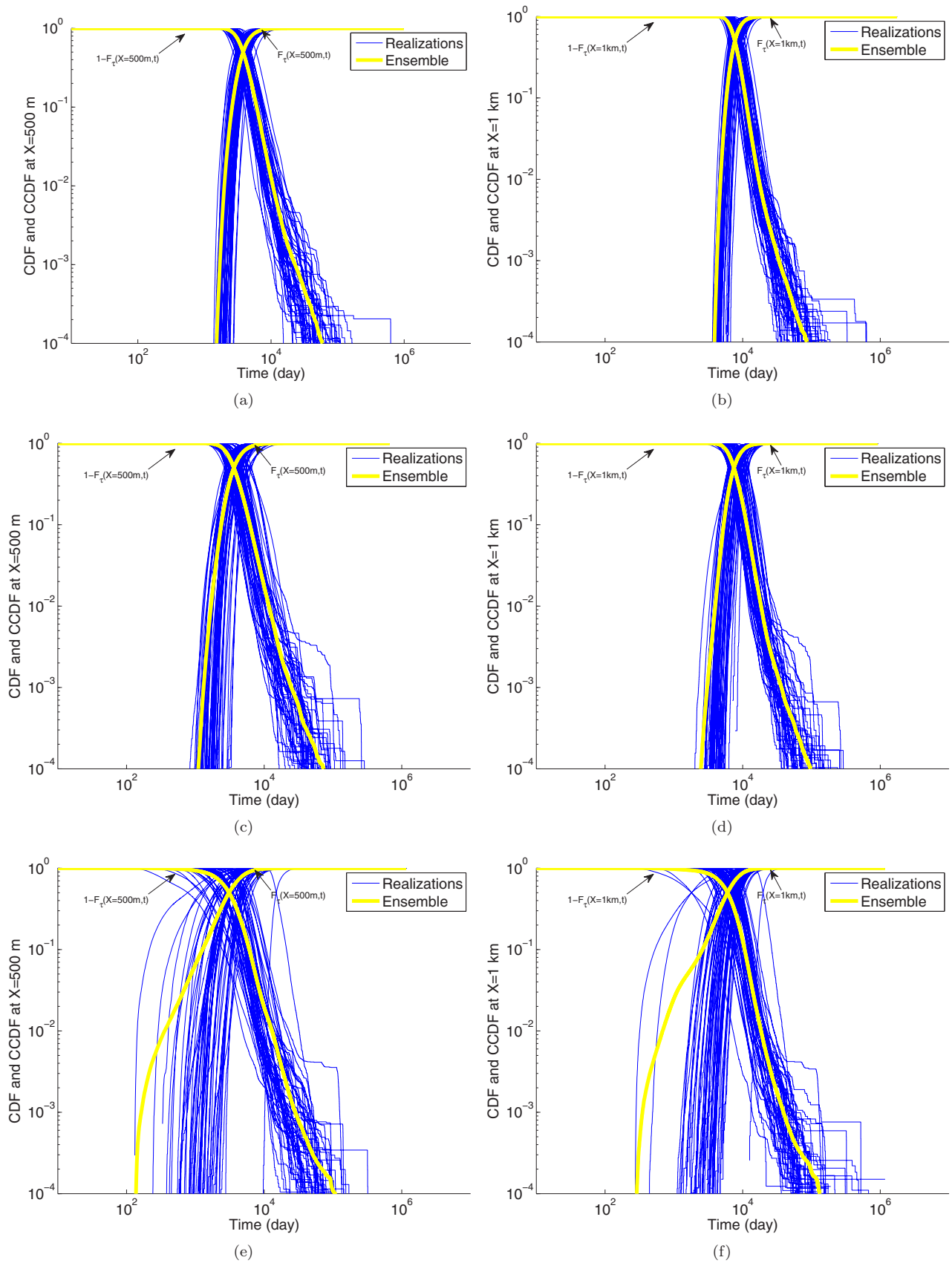


FIG. 15. Cumulative and complementary cumulative travel-time distributions of DFN realizations and the resulting ensemble at (left) $x = 500$ m and (right) $x = 1$ km of large-scale DFN simulations with transmissivity distributions (a, b) $\sigma = 0$, (c, d) $\sigma = 0.5$, and (d, e) $\sigma = 1$.

with the highest errors and all three length scales give similar predictions for total mass in the system. For the most part errors in breakthrough are reduced with larger length scales. For future research, this enables us to eliminate more than two-thirds of the model runs leaving five models and one length scale, allowing us to consider the effects of varying DFN parameters other than transmissivity distribution and to expand model use to three dimensions.

ACKNOWLEDGMENTS

This research was funded by the U.S. Department of Energy under Contracts No. DE-NA-0000939 and No. DE-NA-0003590.

APPENDIX A: NUMBER OF REALIZATIONS

The number of realizations used to create ensemble DFN simulation results was chosen by comparing moments of ensemble breakthrough curves at $X = 1$ km to moments of corresponding breakthrough curves from individual realizations. The moments of the breakthrough curves are defined as

$$\begin{aligned} M_0 &= C_{\text{tot}}(X) = \int_{-\infty}^{\infty} \int_{-\infty}^{\infty} C(x = X, y, t) dy dt, \\ M_1 &= \int_{-\infty}^{\infty} \int_{-\infty}^{\infty} t \frac{C(x = X, y, t)}{C_{\text{tot}}(X)} dy dt, \end{aligned} \quad (\text{A1})$$

where M_0 is the zeroth moment, which measures the total mass arriving at location X , and M_1 is the first moment, which measures the average travel time to location X .

For each realization, we find the relative mean absolute deviation of these moments, defined as

$$\text{rMAD}(\text{real}_j) = \frac{|M_i^{\text{ens}} - M_i^{\text{real}_j}|}{M_i^{\text{ens}}}, \quad (\text{A2})$$

where M_i^{ens} and $M_i^{\text{real}_j}$ are the i th moments of the ensemble and realization, real_j , respectively.

Figure 13 shows the average of these deviations. The number of realizations used to define the ensemble is shown on the x axis. The order in which the realizations are added to the

ensemble is randomized. We define “enough” realizations to be the number of realizations it takes for the relative mean absolute deviations to decrease regularly. Fifty realizations was the number chosen because this standard is met for all values of σ .

APPENDIX B: MEAN-SQUARED LOGARITHMIC ERROR

Here we show the mean-squared logarithmic error (MSLE) of the complimentary cumulative travel-time distributions of the ensemble of each of the upscaled models. This metric is used to further accentuate the error in predictions of late time (tailing) behavior because it weighs errors logarithmically (small errors in small values carry more weight than in rMAE). To calculate the MSLE in the complimentary cumulative travel-time distribution ($1 - F_{\tau}(X, t)$), we discretize time into 100-day increments from 10^4 days up to the longest travel time from the DFN simulations. The reason 10^4 days was selected is because that is approximately where the tailing begins. The error is then defined as

$$\begin{aligned} \text{MSLE}[1 - F_{\tau, \text{mod}}(X)] \\ = \frac{1}{n} \sum_{i=1}^n [\ln(1 - F_{\tau, \text{DFN}}(X, t_i)) - \ln[1 - F_{\tau, \text{mod}}(X, t_i)]]^2, \end{aligned} \quad (\text{B1})$$

where $1 - F_{\tau, \text{DFN}}(X, t_i)$ and $1 - F_{\tau, \text{mod}}(X, t_i)$ are the complimentary cumulative travel-time distributions at time t_i for the DFN and upscaled model simulations, respectively. Figure 14 shows the MSLE for each upscaled model and looks similar to Figs. 9(d) and 10(d), except that the late time overpredictions of the uSMM and SMM for $\sigma = 1$ are more severely penalized.

APPENDIX C: TRAVEL-TIME DISTRIBUTIONS FOR INDIVIDUAL DFN REALIZATIONS

Figure 15 shows the cumulative and complementary cumulative travel-time distributions for each of the DFN realizations along with the distributions of the ensemble.

-
- [1] B. Berkowitz, Characterizing flow and transport in fractured geological media: A review, *Adv. Water Resour.* **25**, 861 (2002).
 - [2] S. P. Neuman, Trends, prospects and challenges in quantifying flow and transport through fractured rocks, *Hydrogeol. J.* **13**, 124 (2005).
 - [3] C. Klimczak, R. A. Schultz, R. Parashar, and D. M. Reeves, Cubic law with aperture-length correlation: Implications for network scale fluid flow, *Hydrogeol. J.* **18**, 851 (2010).
 - [4] R. Liu, B. Li, Y. Jiang, and N. Huang, Mathematical expressions for estimating equivalent permeability of rock fracture networks, *Hydrogeol. J.* **24**, 1623 (2016).
 - [5] G. Margolin, B. Berkowitz, and H. Scher, Structure, flow, and generalized conductivity scaling in fracture networks, *Water Resour. Res.* **34**, 2103 (1998).
 - [6] M. Oda, Permeability tensor for discontinuous rock masses, *Geotechnique* **35**, 483 (1985).
 - [7] T. Chen, C. Clauser, G. Marquart, K. Willbrand, and D. Mottaghy, A new upscaling method for fractured porous media, *Adv. Water Resour.* **80**, 60 (2015).
 - [8] M. R. Sweeney, C. W. Gable, S. Karra, P. H. Stauffer, R. J. Pawar, and J. D. Hyman, Upscaled discrete fracture matrix model (udfm): An octree-refined continuum representation of fractured porous media, *Comput. Geosci.* **24**, 293 (2020).
 - [9] J. D. Hyman, S. Karra, N. Makedonska, C. W. Gable, S. L. Painter, and H. S. Viswanathan, dfnWorks: A discrete fracture network framework for modeling subsurface flow and transport, *Comput. Geosci.* **84**, 10 (2015).
 - [10] S. Painter and V. Cvetkovic, Upscaling discrete fracture network simulations: An alternative to continuum transport models, *Water Resour. Res.* **41**, W02002 (2005).
 - [11] R. Parashar and D. M. Reeves, On iterative techniques for computing flow in large two-dimensional discrete

- fracture networks, *J. Comput. Appl. Math.* **236**, 4712 (2012).
- [12] B. Berkowitz, A. Cortis, M. Dentz, and H. Scher, Modeling non-Fickian transport in geological formations as a continuous time random walk, *Rev. Geophys.* **44**, 1 (2006).
- [13] B. Berkowitz and H. Scher, Anomalous Transport in Random Fracture Networks, *Phys. Rev. Lett.* **79**, 4038 (1997).
- [14] B. Berkowitz and H. Scher, Theory of anomalous chemical transport in random fracture networks, *Phys. Rev. E* **57**, 5858 (1998).
- [15] T. Le Borgne, M. Dentz, and J. Carrera, Spatial Markov processes for modeling Lagrangian particle dynamics in heterogeneous porous media, *Phys. Rev. E* **78**, 026308 (2008).
- [16] R. Benke and S. Painter, Modeling conservative tracer transport in fracture networks with a hybrid approach based on the Boltzmann transport equation, *Water Resour. Res.* **39**, SBH 6-1 (2003).
- [17] P. K. Kang, M. Dentz, T. Le Borgne, and R. Juanes, Spatial Markov Model of Anomalous Transport through Random Lattice Networks, *Phys. Rev. Lett.* **107**, 180602 (2011).
- [18] D. M. Reeves, R. Parashar, G. Pohl, R. Carroll, T. Badger, and K. Willoughby, The use of discrete fracture network simulations in the design of horizontal hillslope drainage networks in fractured rock, *Eng. Geol.* **163**, 132 (2013).
- [19] J. Hyman, M. Dentz, A. Hagberg, and P. K. Kang, Linking structural and transport properties in three-dimensional fracture networks, *J. Geophys. Res.: Solid Earth* **124**, 1185 (2019).
- [20] J. D. Hyman, M. Dentz, A. Hagberg, and P. K. Kang, Emergence of Stable Laws for First Passage Times in Three-Dimensional Random Fracture Networks, *Phys. Rev. Lett.* **123**, 248501 (2019).
- [21] P. K. Kang, J. D. Hyman, W. S. Han, and M. Dentz, Anomalous transport in three-dimensional discrete fracture networks: Interplay between aperture heterogeneity and injection modes, *Water Resour. Res.* **56**, e2020WR027378 (2020).
- [22] T. Sherman, J. Hyman, M. Dentz, and D. Bolster, Characterizing the influence of fracture density on network scale transport, *J. Geophys. Res.: Solid Earth* **125**, e2019JB018547 (2020).
- [23] E. Bonnet, O. Bour, N. E. Odling, P. Davy, I. Main, P. Cowie, and B. Berkowitz, Scaling of fracture systems in geological media, *Rev. Geophys.* **39**, 347 (2001).
- [24] P. Davy, On the frequency-length distribution of the San Andreas fault system, *J. Geophys. Res.: Solid Earth* **98**, 12141 (1993).
- [25] N. E. Odling, Scaling and connectivity of joint systems in sandstones from western Norway, *J. Struct. Geol.* **19**, 1257 (1997).
- [26] C. E. Renshaw, Connectivity of joint networks with power law length distributions, *Water Resour. Res.* **35**, 2661 (1999).
- [27] D. Best and N. I. Fisher, Efficient simulation of the von mises distribution, *J. Roy. Stat. Soc.: Ser. C (Appl. Stat.)* **28**, 152 (1979).
- [28] P. A. Witherspoon, J. S. Wang, K. Iwai, and J. E. Gale, Validity of cubic law for fluid flow in a deformable rock fracture, *Water Resour. Res.* **16**, 1016 (1980).
- [29] B. Berkowitz, C. Naumann, and L. Smith, Mass transfer at fracture intersections: An evaluation of mixing models, *Water Resour. Res.* **30**, 1765 (1994).
- [30] J. Johnson, S. Brown, and H. Stockman, Fluid flow and mixing in rough-walled fracture intersections, *J. Geophys. Res.: Solid Earth* **111**, B12206 (2006).
- [31] P. K. Kang, Q. Lei, M. Dentz, and R. Juanes, Stress-induced anomalous transport in natural fracture networks, *Water Resour. Res.* **55**, 4163 (2019).
- [32] N. Makedonska, S. L. Painter, Q. M. Bui, C. W. Gable, and S. Karra, Particle tracking approach for transport in three-dimensional discrete fracture networks, *Comput. Geosci.* **19**, 1123 (2015).
- [33] A. Cortis and B. Berkowitz, Computing “anomalous” contaminant transport in porous media: The CTRW MATLAB toolbox, *Ground Water* **43**, 947 (2005).
- [34] M. Dentz, H. Scher, D. Holder, and B. Berkowitz, Transport behavior of coupled continuous-time random walks, *Phys. Rev. E* **78**, 041110 (2008).
- [35] D. Bolster, Y. Méheust, T. L. Borgne, J. Bouquain, and P. Davy, Modeling preasymptotic transport in flows with significant inertial and trapping effects—The importance of velocity correlations and a spatial Markov model, *Adv. Water Resour.* **70**, 89 (2014).
- [36] N. Sund, D. Bolster, S. Mattis, and C. Dawson, Preasymptotic transport upscaling in inertial and unsteady flows through porous media, *Transp. Porous Media* **109**, 411 (2015).
- [37] A. Cortis and J. Birkholzer, Continuous time random walk analysis of solute transport in fractured porous media, *Water Resour. Res.* **44**, W06414 (2008).
- [38] Y. Edery, S. Geiger, and B. Berkowitz, Structural controls on anomalous transport in fractured porous rock, *Water Resour. Res.* **52**, 5634 (2016).
- [39] S. Geiger, A. Cortis, and J. Birkholzer, Upscaling solute transport in naturally fractured porous media with the continuous time random walk method, *Water Resour. Res.* **46**, W12530 (2010).
- [40] S. Geiger and S. Emmanuel, Non-fourier thermal transport in fractured geological media, *Water Resour. Res.* **46**, W07504 (2010).
- [41] T. Sherman, N. B. Engdahl, G. Porta, and D. Bolster, A review of spatial Markov models for predicting pre-asymptotic and anomalous transport in porous and fractured media, *J. Contam. Hydrol.* **236**, 103734 (2020).
- [42] P. K. Kang, M. Dentz, T. Le Borgne, S. Lee, and R. Juanes, Anomalous transport in disordered fracture networks: Spatial Markov model for dispersion with variable injection modes, *Adv. Water Resour.* **106**, 80 (2017).
- [43] P. K. Kang, T. Le Borgne, M. Dentz, O. Bour, and R. Juanes, Impact of velocity correlation and distribution on transport in fractured media: Field evidence and theoretical model, *Water Resour. Res.* **51**, 940 (2015).